# Effects of the Opening Speed of the Valve in a Diaphragmless Shock Tube for Metrological Purposes

Francisco Javier Hernández Castro, Jože Kutin, and Andrej Svete

***Abstract*—To develop a measurement system for calibrating high-frequency dynamic pressure that is capable of acting as a primary dynamic pressure calibration standard, a new concept of the shock tube, called the diaphragmless shock tube, has recently been developed. In most such shock tubes, the diaphragm is replaced with a commercially available, ISTA KB fast-opening valve (FOV). In this article, a numerical model was built in OpenFOAM to investigate the effects of the opening mechanism of ISTA KB-40-100 FOV on the formation of the shock wave in a shock tube with an internal radius of 20 mm. Numerical simulations were performed for the driver-driven pressure ratio of 40 and the valve-opening speeds of 5, 10, and 20 m/s, which were compared with the case of instantaneous valve opening, and the results predicted by the ideal shock tube theory. The observed variables were the mass flow through the valve, as well as the pressure, the temperature, and the shock wave velocity in the formation region behind the valve. The results show that when the shock wave undergoes an initial acceleration, the shock front accelerates more at higher opening speeds of the valve. The results also show that the valve-opening mechanism generates a series of reflection waves that propagate into the driven section, giving the shock wave velocity an oscillatory character, which can affect the calibration and measurement capability of the shock tube as a primary high-frequency, time-varying, pressure calibration standard.**

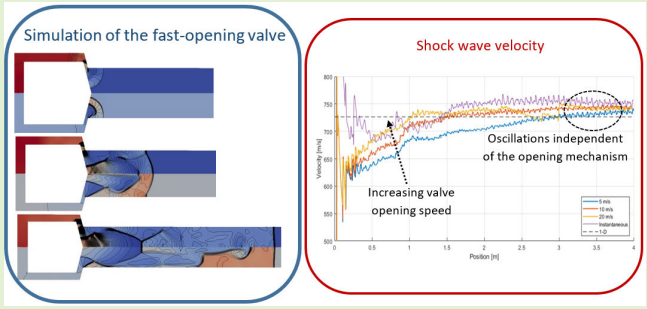


***Index Terms*— Diaphragmless shock tube, numerical simulations, OpenFOAM, primary calibration method, shock wave formation, time-varying pressure.**

## I. Introduction

SUPERSONIC aircraft, explosions, lightning, and other phenomena that release energy suddenly can produce shock waves. Shock waves in gases are an exceptionally thin boundary that propagates at supersonic speeds, resulting in an increase in pressure, density, temperature, and flow velocity [1]. For these reasons, shock waves have always been considered a fascinating natural phenomenon that has motivated numerous research efforts over the years, providing a lot of scientific knowledge in various fields, such as aerospace [2], [3], [4], automotive [5], geophysics [6], and medicine [7].

Shock tubes are devices capable of generating shock waves in a controlled manner and are therefore suitable for studying the changes in the properties of gases caused by the propagation of these shock waves. In general, shock tubes consist of two sections: the high-pressure driver section with an initial uniform pressure $p_4$ and temperature $T_4$ and the low-pressure driven section with an initial uniform pressure $p_1$ and temperature $T_1$. These sections are initially separated by a physical element [see Fig. 1(a)]. When the separation element is instantly removed, the interaction between the two sections generates a shock wave that propagates into the driven section and divides the shock tube into four main regions [see Fig. 1(b)]. The shock wavefront increases the pressure of the gas upstream $p_1$ to $p_2$, whereas the pressure across the interface between the driver and the driven gas, known as the contact surface, is preserved, $p_3 = p_2$. The contact surface represents the boundary between the high-temperature region, which extends to the shock wavefront upstream of the contact surface, and the low-temperature region, which extends to the

Manuscript received 19 October 2023; accepted 13 November 2023. Date of publication 22 November 2023; date of current version 2 January 2024. This work was supported in part by the Slovenian Research and Innovation Agency for the project Advanced Shock Tube System for High-Frequency Primary Dynamic Pressure Calibration under project J2-3054 and in part by the research core funding under grant P2-0223. The associate editor coordinating the review of this article and approving it for publication was Dr. Cheng-Sheng Huang. *(Corresponding author: Andrej Svete.)*

The authors are with the Laboratory of Measurements in Process Engineering, Faculty of Mechanical Engineering, University of Ljubljana, 1000 Ljubljana, Slovenia (e-mail: javier.hernandez-castro@fs.uni-lj.si; joze.kutin@fs.uni-lj.si; andrej.svete@fs.uni-lj.si).

Digital Object Identifier 10.1109/JSEN.2023.3333323

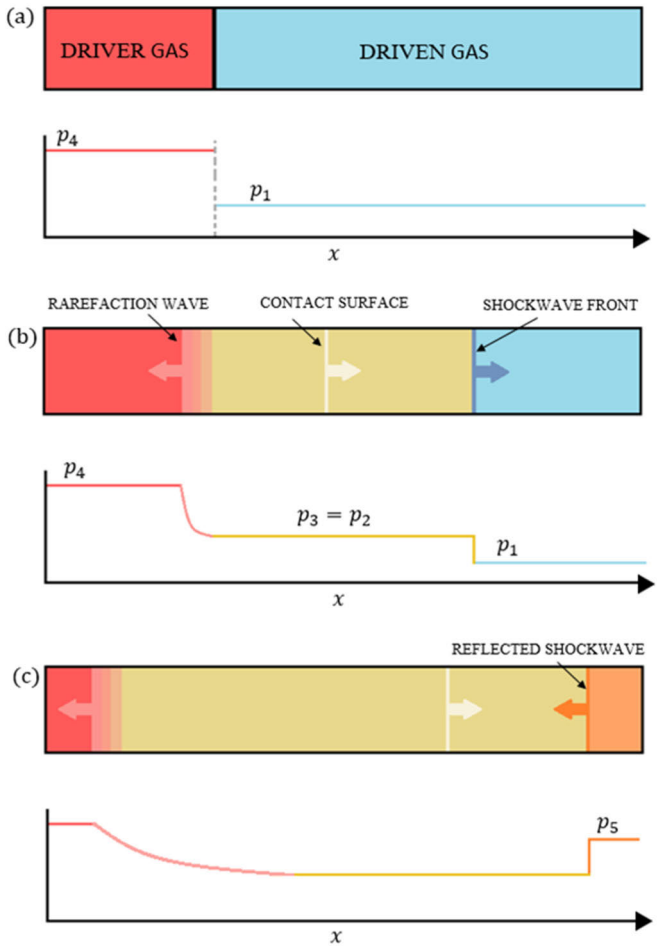


Fig. 1. Operation of the shock tube, (a) Driver and driven sections separated by a physical element, (b) shock wave propagating into the driven section, and (c) shock wave reflected from the end wall.

rarefaction wave downstream of the contact surface. When the shock wave reaches the end of the driven section, it is reflected from the end wall, causing the pressure to increase to $p_5$ [see Fig. 1(c)]. The amplitude of the pressure step change upon reflection of the shock front can be calculated as [8], [9], [10]

$$\Delta p = 2p_1 \frac{\gamma_1}{\gamma_1^2 - 1}(M_s^2 - 1)\left(\frac{M_s^2(3\gamma_1 - 1) + 3 - \gamma_1}{M_s^2 + \frac{2}{\gamma_1 - 1}}\right) \quad (1)$$

where $\gamma_1$ is the adiabatic index of the driven gas, $M_s = W/a_1$ is the shock wave Mach number at the end wall, where $W$ is the velocity of the shock wave, $a_1 = (\gamma_1 R_1 T_1)^{1/2}$ is the speed of sound in the driven gas, and $R_1$ is its specific gas constant. The pressure change caused by the reflection of the shock wave from the end wall of the driven section can be considered to be an almost ideal step change with a rise time of the order of 1 ns [11]. This makes shock tubes suitable for the calibration of sensors for high-frequency dynamic pressure changes, which are used in a wide range of applications in the aerospace and automotive industries, robotics, and production engineering [12], [13], [14], [15], [16], [17], [18], [19], [20]. Furthermore, it is clear from (1) that the metrological traceability of time-varying pressure is established by the measurements of $p_1$, $T_1$, and $W$ determined by the time-of-flight (TOF) method, which makes the shock tube an ideal candidate for a primary high-frequency, time-varying, pressure calibration standard.

Shock tubes can be classified in terms of the separation element used for the generation of the shock waves into diaphragm and diaphragmless shock tubes. In diaphragm shock tubes, the shock waves are generated by the bursting of the diaphragm, which initially separates the driver and driven sections. The shock wave formation is influenced by the properties and material of the diaphragm, leading to large uncertainties in the repeatability of the generated shock waves [21], [22]. Furthermore, the often present incomplete ruptures of the diaphragm lead to generated pressure steps with lower amplitudes than envisaged by the ideal shock tube theory [23], [24]. The rupture of the diaphragm also pollutes the test section with solid particles that can affect or even damage the pressure sensors being calibrated [25], [26]. The fact that the diaphragms must be replaced after each test, which requires disassembly and reassembly of the shock tube, affects the economics of the system and thus the viability of this pressure standard [27]. Therefore, in recent years, conventional shock tubes with a diaphragm are being replaced by diaphragmless shock tubes with a fast-opening valve (FOV). Diaphragmless shock tubes pose a technical challenge for the design and manufacture of an FOV with an opening time comparable to that of a bursting diaphragm, which is of the order of a few tenths of a millisecond [25]. The longer opening times of the FOV in comparison to the bursting diaphragms result in longer distances at which the shock wave reaches its maximum velocity, i.e., the formation distances, and therefore longer driven sections compared to conventional diaphragm shock tubes [28]. An FOV commonly used in diaphragmless shock tubes for dynamic pressure calibrations is a commercially available ISTA KB valve [9], [27], [29], [30], [31], [32], [33], [34], [35], [36]. The FOV is actuated by an electropneumatic valve that, when activated, vents the pressurized gas from the FOV, causing the FOV to slide toward the driver section, allowing the driver and driven gases to interact.

This article determines the effects of the opening mechanism of the ISTA KB-40-100 FOV on the formation of the shock waves. Numerical simulations were performed in OpenFOAM by upgrading a preliminary study in [37] with the inclusion of the motion of the valve geometry. Three different opening speeds of the FOV based on its opening distances and times specified by the manufacturer were investigated and compared with an ideal instantaneous valve opening and the results predicted by the ideal shock tube theory. In these simulations, the mass flow through the valve and the pressure, temperature and the velocity of the shock wave in the formation region behind the valve were analyzed. For estimating the velocity of the shock wave, an improved method based on the pressure evolution inside the computational elements, which enables an improved spatial resolution of one computational cell, was developed.

This article is structured as follows. Section II presents the problem setup, including the geometry, boundary and initial conditions, governing equations, mesh, and solver. Section III

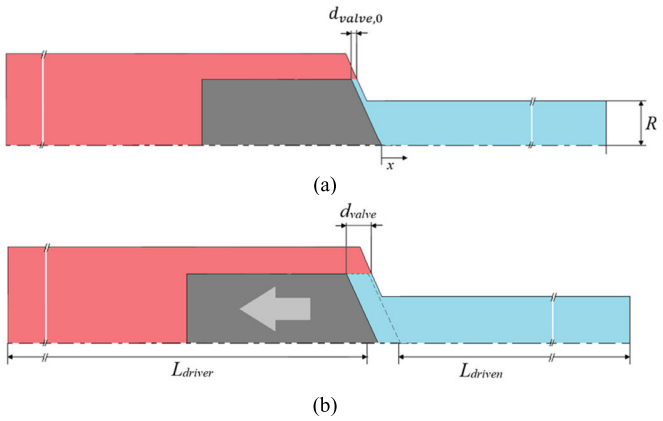


Fig. 2. Schematic side view of the simulated diaphragmless shock tube (a) with the FOV closed and (b) after opening the FOV in the direction of the gray arrow. The dimensions are not to scale.

describes the methodology for estimating the mass flow rate through the FOV. Furthermore, a newly developed method for estimating the shock wave velocity in the driven section and its validation is presented. Section IV presents the results of the mass flow rate through the FOV, and the pressure, temperature, and the shock wave velocity in the formation region, as well as a frequency analysis of the numerically obtained pressure signals. Section V summarizes the conclusion.

## II. Problem Description

### A. Geometry

The geometry of the problem is a simplification of the geometry of the ISTA KB-40-100 FOV. As can be seen in Fig. 2, the driver (in red) and driven (in blue) sections are initially separated by the FOV (in gray). To ensure the stability of the simulations, the valve cannot be completely closed at the initial time. Therefore, the initial value of the gap opening $d_{\text{valve},0}$ was set to 2 mm, which allows a reasonable number, in terms of time consumption, of remeshings, as described in Section II-E. At the moment of activation, the FOV with the 52.77° angle cone of the length of 19 mm moves into the driver section, as indicated by the gray arrow. This opens a gap between the driver and driven sections and the high-pressure gas can flow into the latter. The final FOV opening distance $d_{\text{valve}} = 13$ mm, which corresponds to the actual maximum opening distance of the ISTA KB-40-100 FOV. The length of the driver section $L_{\text{driver}} = 1$ m and the tube radius $R = 20$ mm correspond to the actual diaphragmless shock tube with an implemented ISTA KB-40-100 FOV, which was developed in the Laboratory of Measurements in Process Engineering (LMPS), University of Ljubljana, Ljubljana, Slovenia. However, since only the section of shock wave formation behind the valve is of interest, the length of the driven section $L_{\text{driven}}$ was shortened to 4 m in the simulations.

### B. General Assumptions and Boundary Conditions

The manufacturer of the FOV under investigation specifies its opening time as about 1–2 ms. Based on this data, three different opening speeds of 5, 10, and 20 m/s were simulated, corresponding to opening times of 2.6, 1.3, and 0.65 ms, respectively. An additional simulation was performed assuming an instantaneous valve opening to determine the maximum shock wave velocity that the shock tube can generate under the given initial conditions. The boundary conditions considered are adiabatic walls of the shock tube, zero flow velocity at the walls, and zero pressure gradient in the direction normal to the walls. The problem was modeled as 2-D axisymmetric.

### C. Initial Conditions

At the initial time, the fluid was assumed to be uniformly at rest throughout the whole domain and the ambient temperature was assumed to be uniformly 300 K. The initial pressure in the driver section $p_4$ was set to 4 MPa and the initial pressure in the driven section $p_1$ was set to 0.1 MPa, as these correspond to the actual pressure conditions in the shock tube under consideration. At the initial time, the driver and driven sections are separated by the FOV, as shown in Fig. 2(a). The gas considered in the simulations was nitrogen, the thermophysical properties of which were determined using the REFPROP database [38] at a reference temperature of 300 K and pressure 0.1 MPa. Nitrogen has a molecular weight $M$ of 28.013 g/mol, a heat capacity at a constant pressure $C_p$ of 1037.9 J/kg·K, and at a constant volume $C_v$ of 741.1 J/kg·K.

### D. Governing Equations

The equations to be solved are the Navier–Stokes conservation equations for gases. Applying the aforementioned assumptions, these equations reduce to Euler's equations, which have the form

$$\frac{\partial \rho}{\partial t} + \nabla \cdot (\rho \boldsymbol{U}) = 0 \tag{2}$$

$$\frac{\partial (\rho \boldsymbol{U})}{\partial t} + \nabla \cdot (\rho \boldsymbol{U}\boldsymbol{U}) = -\nabla p + \nabla \cdot \underline{\boldsymbol{\tau}} \tag{3}$$

$$\frac{\partial (\rho e_s)}{\partial t} + \nabla \cdot [\boldsymbol{U}(\rho e_s)] + \nabla q + \nabla \cdot \left( \left( p\boldsymbol{I} - \underline{\boldsymbol{\tau}} \right) \boldsymbol{U} \right) = 0 \tag{4}$$

where $\rho$ is the density, $\boldsymbol{U}$ is the velocity vector field, $\underline{\boldsymbol{\tau}}$ is the viscous stress tensor, $e_s$ is the sensible internal energy, $q$ is the heat-flux density, and $\boldsymbol{I}$ is the identity matrix. $\underline{\boldsymbol{\tau}}$ can be expressed as

$$\underline{\boldsymbol{\tau}} = 2\mu \text{dev}\left(\underline{\boldsymbol{D}}\right) \tag{5}$$

where $\underline{\boldsymbol{D}} = (1/2)[\nabla \boldsymbol{U} + (\nabla \boldsymbol{U})^T]$ is the deformation gradient tensor, $\text{dev}(\underline{\boldsymbol{D}}) = \underline{\boldsymbol{D}} - (1/3)\text{tr}(\underline{\boldsymbol{D}})\boldsymbol{I}$ is its deviator component, and $\mu$ is the dynamic viscosity, which is calculated according to Sutherland's law as

$$\mu = \frac{A_s \sqrt{T}}{1 + \frac{T_s}{T}} \tag{6}$$

where the coefficients $A_s = 1.400979806 \cdot 10^{-6}$ kg/(m·s·$\sqrt{K}$) and $T_s = 107$ K for nitrogen were taken from [39]. The heat-flux density is described by Fourier's law as $q = -\lambda T$, where $\lambda$ is the thermal conductivity, which is calculated according to the modified Eucken correlation for polyatomic gases [40]

$$\lambda = \mu C_v \left( 1.32 + 1.77 \frac{R}{C_v} \right). \tag{7}$$

TABLE I
NUMBER OF COMPUTATIONAL ELEMENTS

| Meshing | Number of cells |
|---|---|
| 1st meshing | 168066 |
| 2nd meshing | 169472 |
| 3rd meshing | 171988 |
| 4th meshing | 246894 |

The nitrogen was assumed to be a perfect gas; therefore, the following relations apply:

$$e_s = \big(C_p - R\big)T = C_v T \tag{8}$$

$$p = \rho R T. \tag{9}$$

### E. Numerical Model

The mesh along the entire length of the driven section was uniform with hexahedral cells of size $0.5 \times 0.5$ mm$^2$, although it was refined near the valve. Such a mesh size is not sufficient to properly capture the viscous effects near the driven section walls, which would require mesh refinement in the radial direction toward the wall. However, it was shown in [41] that the shock wave formation is dominated by the interactions of the shock waves and the reflections from the tube wall, so that the role of viscous effects near the wall is negligible. The influence of the mesh refinement on the results is analyzed in Section IV-A.

The motion of the mesh was calculated using a solver integrated in OpenFOAM, which calculates the velocity field $\boldsymbol{U}_m$ of the mesh points by solving Laplace's equation [42]

$$\nabla \cdot (\delta \nabla \boldsymbol{U}_m) = 0 \tag{10}$$

where $\delta$ is the diffusivity parameter that controls how the mesh movement is distributed through the mesh and, for a given cell in the opening gap, was inversely proportional to the square of the distance to the valve walls. The boundary conditions for this equation take into account that all the boundaries are stationary, except for the wall of the FOV, the velocity of which in the axial direction is constant and negative. After solving (10), the mesh is modified as

$$r_{j+1} = r_j + \boldsymbol{U}_m \Delta t \tag{11}$$

where $r_j$ are the positions of the mesh points for a given time step.

To avoid excessive deformation of the mesh in the opening gap, the geometry of the moving cases had to be remeshed when the elongation of the cells in the valve-opening-gap region exceeded 1 mm in the longitudinal direction, resulting in three remeshings. The number of computational elements in each mesh is given in Table I.

Fig. 3 shows the mesh and its dynamic boundary conditions after each of the remeshings. The moving part of the FOV and its direction of movement are highlighted in red, the stationary walls of the tube are highlighted in green, whereas the axis of the tube is highlighted in black. The influence that the mesh had on the results is investigated and presented in Section IV.

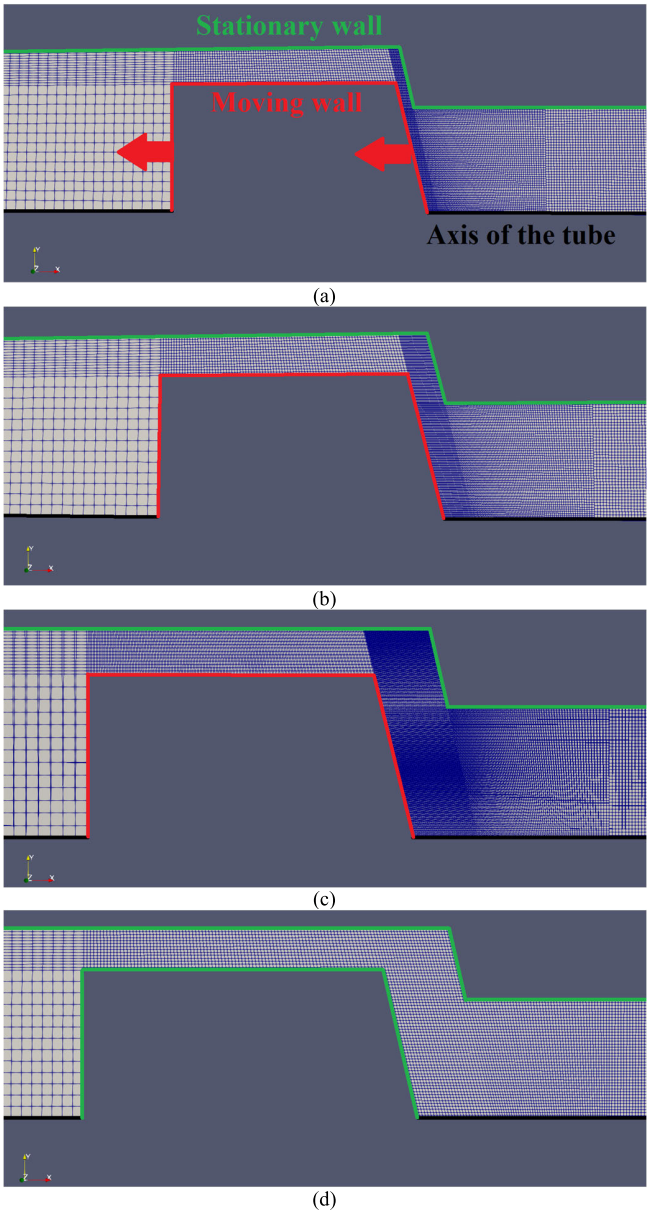


Fig. 3. Rendering of the mesh around the FOV from the initial position (a) to the fully open position, (d) after applying the necessary remeshings for valve-opening distances of (b) 5 and (c) 10 mm.

### F. Solver

The simulations were carried out in OpenFOAM using the rhoCentralFoam solver for compressible flows. This solver was chosen because it was shown in [43] that the solver locates the shock wavefront with better accuracy than other solvers for compressible flows in OpenFOAM, such as sonicFoam. rhoCentralFoam is a density-based solver constructed on the principle that properties are transported not only by the flow itself but also by the propagation of the waves. The convective terms in (2) to (4) in the form $\nabla \cdot (\rho \boldsymbol{U})$, $\nabla \cdot (\rho \boldsymbol{U}\boldsymbol{U})$, $\nabla \cdot [\boldsymbol{U}(\rho e_s)]$, and $\nabla \cdot (p\boldsymbol{I}\boldsymbol{U})$ are integrated over the control volume and linearized to obtain the fluxes for each cell face. The interpolation schemes use the limiting function proposed by Van Albada et al. [44]. The maximum Courant–Friedrichs–Lewy (CFL) number was limited to 0.2 to ensure the stability of the calculations.

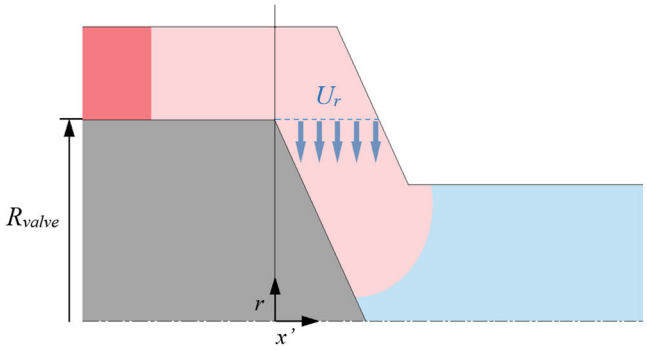


Fig. 4. Schematic side view of the mass flow through the valve opening gap.

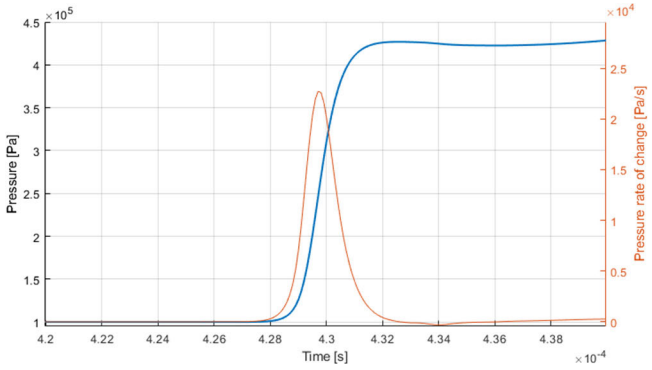


Fig. 5. Pressure (blue) and pressure rate of change (orange) on the axis of the tube, 0.5-m downstream of the FOV.

## III. Postprocessing Methodology

### A. Determination of the Mass Flow Rate Through the Valve

The mass flow through the valve gap, as shown in Fig. 4, at a radial distance from the axis equal to $R_{\text{valve}}$, was calculated as

$$q_m = 2\pi R_{\text{valve}} \int_0^{d_{\text{valve}}} \rho(x,t) \boldsymbol{U}_r(x',t) dx \tag{12}$$

which after the application of spatial and temporal discretization has the form

$$q_{m_j} = 2\pi R_{\text{valve}} \sum_{i=1}^{n_x} \rho_{i,j} \boldsymbol{U}_{r_{i,j}} \Delta x_{i,j} \tag{13}$$

where the index $i$ refers to the number of the cells along the longitudinal direction $x'$ and the index $j$ to the number of respective time steps.

### B. Determination of the Shock Wave Velocity

The velocity of the shock wave was calculated based on the variation of the pressure along the driven section of the shock tube. The shock wave was assumed to cross the center of a particular cell when the rate of change of the pressure in that cell was the highest. Fig. 5 shows the pressure signal and its rate of change $\Delta p/\Delta t$ in the cell 0.5-m downstream of the FOV on the central axis of the tube.

The procedure for determining the shock wave velocity is shown in Fig. 6. The values of the rate of change of pressure

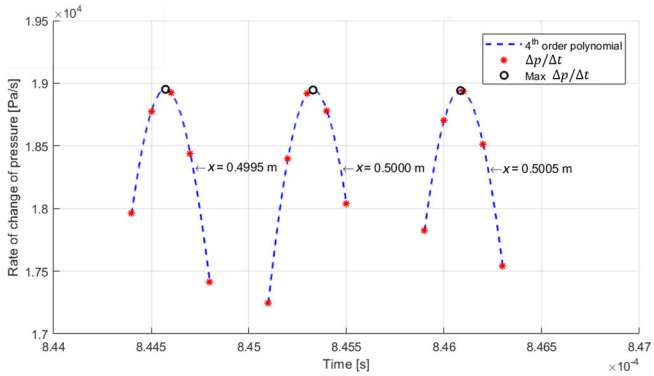


Fig. 6. Rate of change of pressure approximated using a fourth-order polynomial around its maximum for three consecutive cells in the driven section.

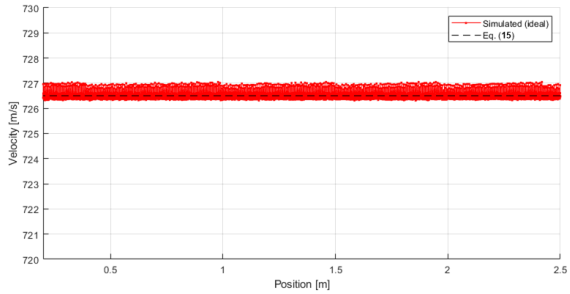


Fig. 7. Comparison of the shock wave velocity calculated with the method considered and the velocity predicted by the ideal shock tube theory.

obtained with the sampling frequency of 10 MHz in three consecutive cells are marked with the red asterisks, which were fitted with a fourth-order polynomial fit (blue dashed lines) to obtain the maximum values of the rate of change (black circle). The time of this maximum $t_i$ in each cell was considered as the time when the shock wave crossed the center of the cell $x_i$. The shock wave velocity at the midpoint between the centers of cell $i$ and cell $i+1$ was then determined as

$$W_i = \frac{x_{i+1} - x_i}{t_{i+1} - t_i}. \tag{14}$$

The presented method for estimating the shock wave velocity was verified by applying it to a simulation of a 1-D shock tube, where the full bore separation element was instantaneously removed and the same input parameters as described in Section II were considered. In this case, the calculated shock wave velocity can be compared to the velocity predicted using the ideal shock tube theory as [45]

$$W = a_1 \sqrt{\frac{\gamma+1}{2\gamma}\left(\frac{p_2}{p_1} - 1\right) + 1} \tag{15}$$

where $p_2$ can be solved implicitly using

$$\frac{p_4}{p_1} = \frac{p_2}{p_1}\left[1 - \frac{a_1}{a_4}\left(\frac{p_2}{p_1} - 1\right)\frac{\gamma-1}{\sqrt{2\gamma\left(2\gamma + (\gamma+1)\left(\frac{p_2}{p_1} - 1\right)\right)}}\right]^{\frac{-2\gamma}{\gamma-1}}. \tag{16}$$

Fig. 7 shows that the shock wave velocity calculated using the method considered agrees very well with the shock wave

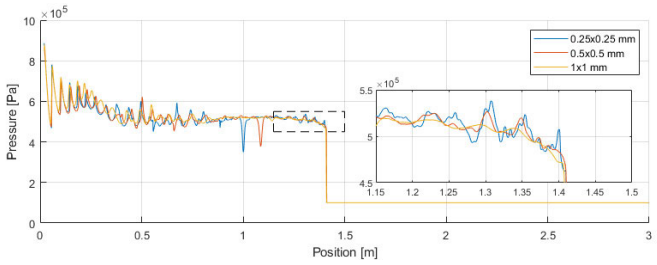


Fig. 8. Pressure distribution along the wall at $t = 0.002$ s for the different meshes applied for the case of instantaneous valve opening.

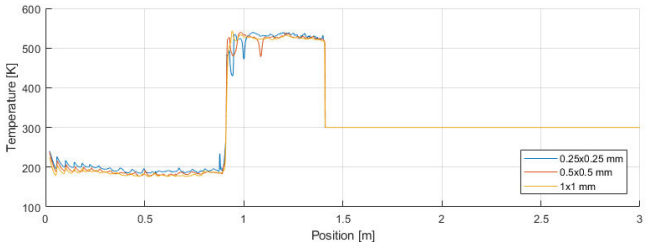


Fig. 9. Temperature distribution along the wall at $t = 0.002$ s for the different meshes applied for the case of instantaneous valve opening.

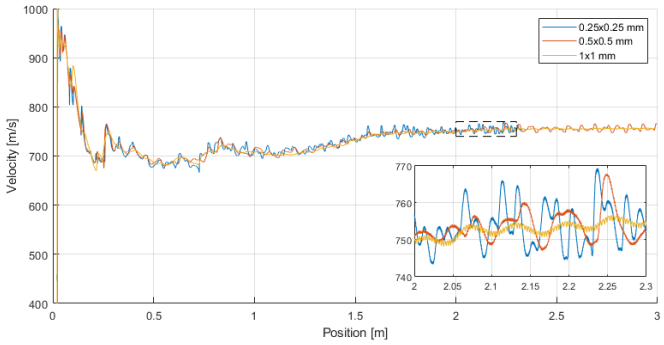


Fig. 10. Shock wave velocity along the wall for the three levels of mesh refinement.

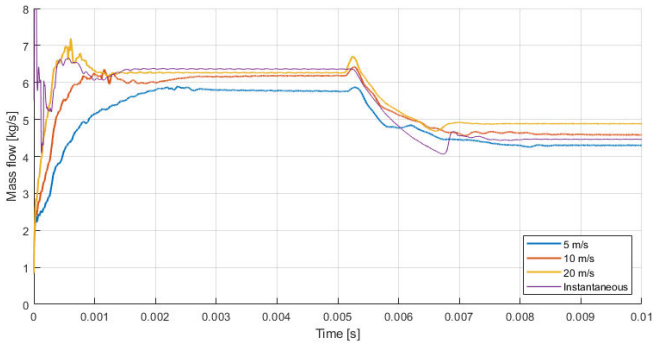


Fig. 11. Mass flow through the FOV.

velocity predicted using the ideal shock tube theory. The relative difference between them is on average less than 0.08%.

## IV. Results

### A. Spatial and Temporal Resolution Study

To validate the influence of the mesh on the results, the case with the instantaneous valve opening was simulated with three refinement levels of the mesh applied to the driven section. The computational elements of this mesh were hexahedral, uniform, and had sizes of $0.25 \times 0.25$, $0.5 \times 0.5$, and $1 \times 1$ mm$^2$, respectively. Note that changes in spatial resolution also entail changes in temporal resolution, as these two are linked by the CFL condition. This resulted in simulation time steps of $8.33 \cdot 10^{-9}$, $1.67 \cdot 10^{-8}$, and $1.25 \cdot 10^{-8}$ s, respectively. To obtain sufficient pressure data for the estimation of the shock wave velocity, the sampling periods were $0.5 \cdot 10^{-7}$, $1 \cdot 10^{-7}$, and $2.5 \cdot 10^{-7}$ s, respectively.

The effects of discretization on the shock wave formation were studied by observing the pressure and temperature distributions along the driven section downstream of the valve. The longitudinal pressure and temperature distributions in the driven section represented in Figs. 8 and 9, respectively, show different regions into which the shock wave divides the shock tube. If we look at the details in Fig. 8, we see that the shock wavefront is followed by a series of pressure oscillations that are better captured by the $0.5 \times 0.5$ and $0.25 \times 0.25$ mm$^2$ meshes. Since the method for estimating the shock wave velocity is based on pressure, it is expected that these pressure variations have an impact on the shock wave velocity results.

Fig. 10 shows that the obtained trend in shock wave velocity is similar for all meshes. However, the shock wave velocity shows an oscillatory character that is not as evident for the $1 \times 1$ mm$^2$ mesh as for the other two, which could be a result of undersampling. As the simulation run with the $0.25 \times 0.25$ mm$^2$ mesh is significantly more computationally costly than that with the $0.5 \times 0.5$ mm$^2$ mesh and at the same time giving comparable results, the latter was chosen in this study.

### B. Mass Flow Through the FOV

The mass flow through the FOV opening gap in general increases in proportion to the opening speed of the valve until it reaches a steady maximum value, as shown in Fig. 11. In the case of the 20-m/s opening and the instantaneous opening additional peak in mass flow occurs in the first millisecond due to the vortex being generated by the gas flow around the FOV. After reaching a steady value, the mass flow remains constant until the expansion wave reflected from the end wall of the driver section reaches the FOV, resulting in a decrease in mass flow at about 5.25 ms. The results also show that the maximum mass flow depends on the opening speed of the valve, which is higher for faster openings.

### C. Pressure and Temperature Along the Driven Section

Figs. 12–14 show the pressure and temperature contours during the first 0.5 ms of the valve opening, for a shock wave formed by opening the valve at a speed of 5, 10, and 20 m/s, respectively. Figs. 12(a), 13(a), and 14(a) show that the pressure difference between the driver and the driven gas and the geometry of the valve generate a toroidal shock wave in the first moments, which converges toward the central axis of the tube. The mechanism of such a shock wave was studied in detail in [46] and results in an amplification of the shock wave upon reflection from the axis, as shown in Figs. 12(b), 13(b), and 14(b). Subsequently, the leading shock is projected toward the walls, where it was reflected and

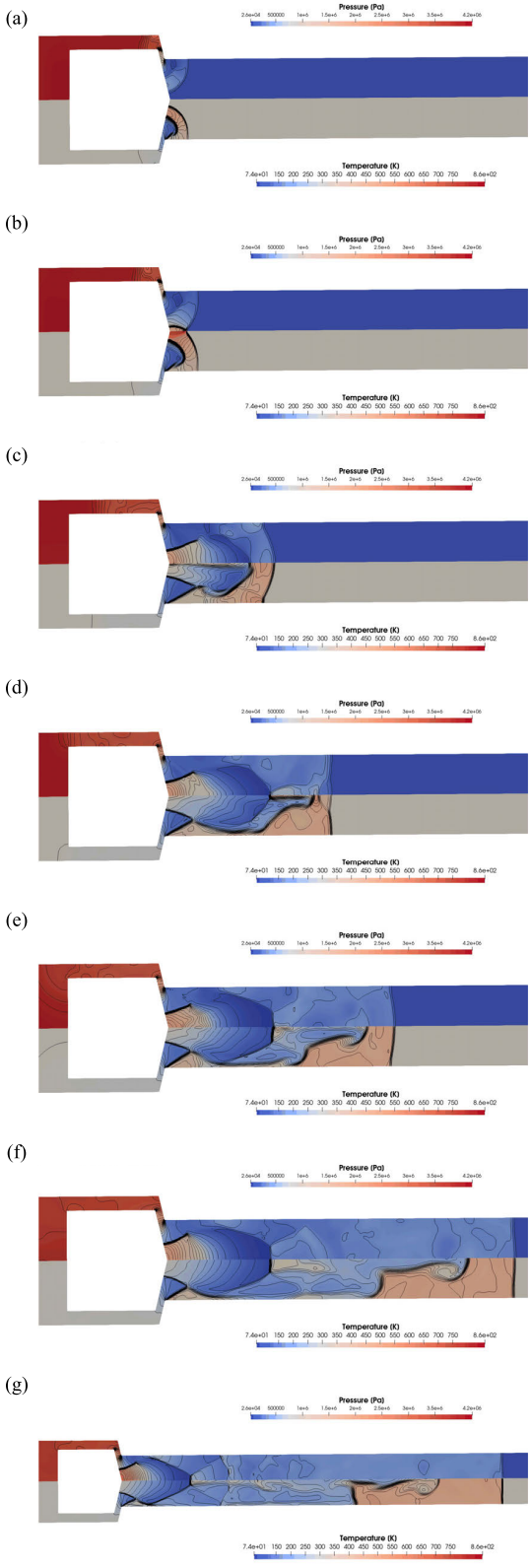


Fig. 12. Pressure and temperature contours during first 0.5 ms after opening of the valve at a speed of 5 m/s. (a) $t = 0.03$ ms, (b) $t = 0.04$ ms, (c) $t = 0.10$ ms, (d) $t = 0.15$ ms, (e) $t = 0.20$ ms, (f) $t = 0.30$ ms, and (g) $t = 0.50$ ms.

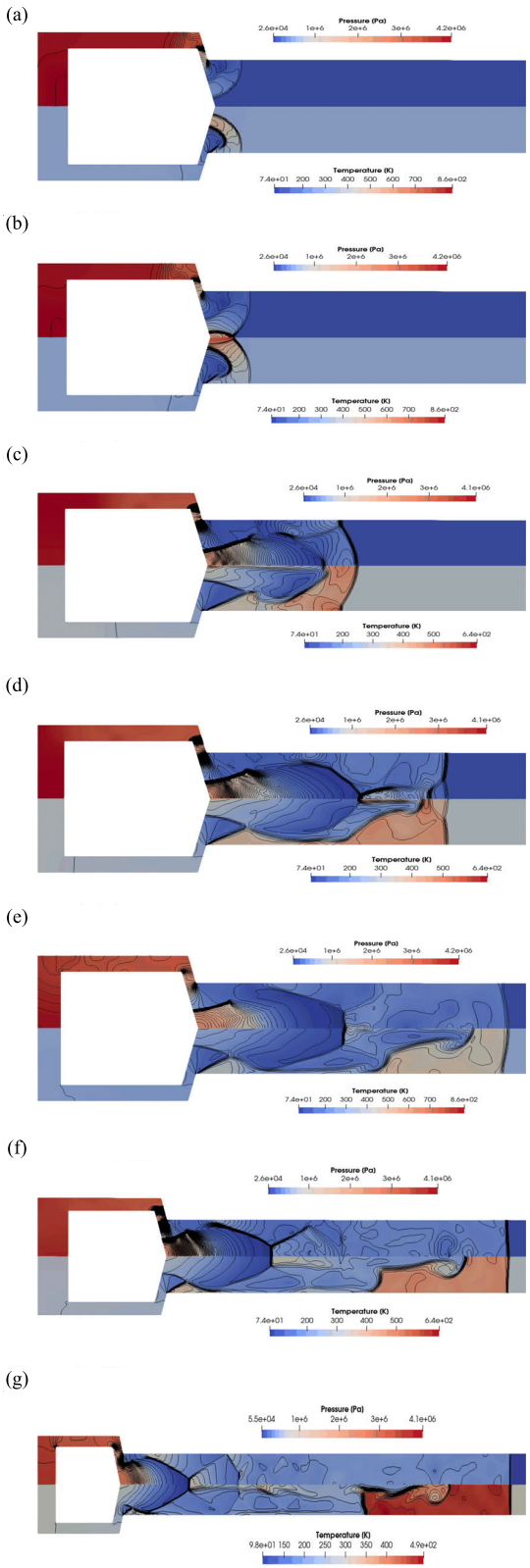


Fig. 13. Pressure and temperature contours during first 0.5 ms after opening of the valve at a speed of 10 m/s. (a) $t = 0.03$ ms, (b) $t = 0.04$ ms, (c) $t = 0.10$ ms, (d) $t = 0.15$ ms, (e) $t = 0.20$ ms, (f) $t = 0.30$ ms, and (g) $t = 0.50$ ms.

evolved into a lambda shock, which can be seen in Figs. 12(c), 13(c), and 14(c). The triple point of the lambda shock focuses toward the axis of the tube [see Figs. 12(d), 13(d), and 14(d)] and coalesces into the leading shock [see Figs. 12(e), 13(e), and 14(e)]. Figs. 12(e)–(g), 13(e)–(g), and 14(e)–(g) show that the leading shock becomes planar and perpendicular to the

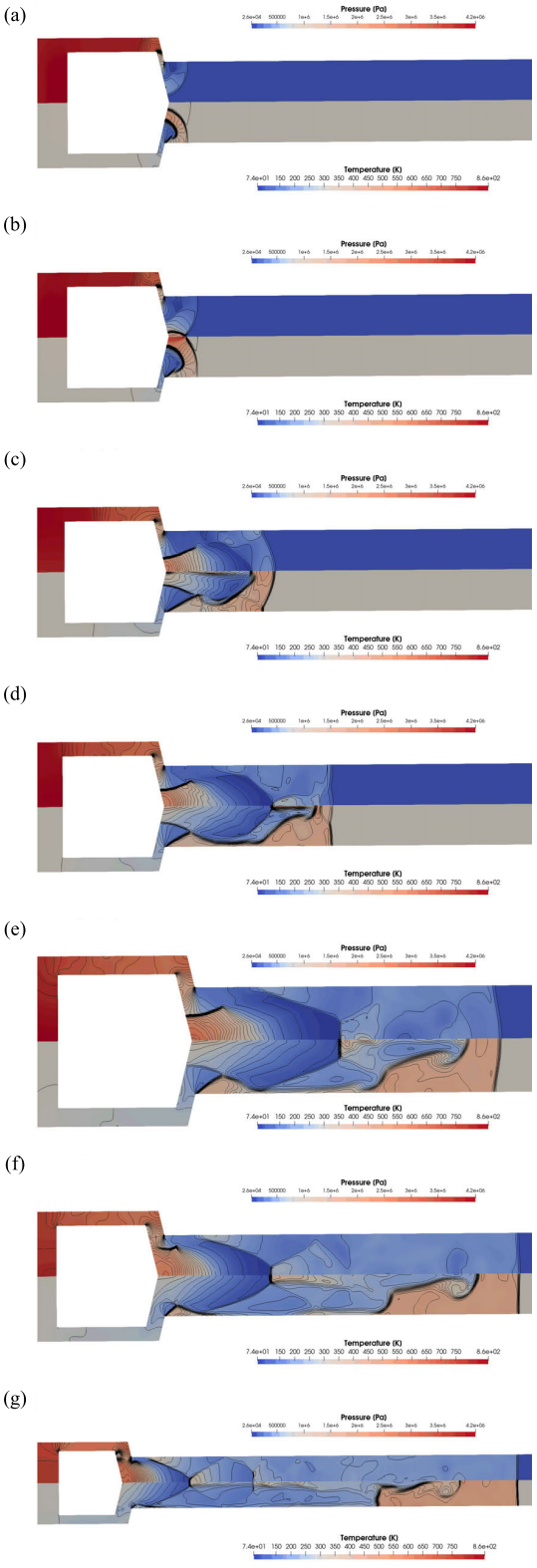


Fig. 14. Pressure and temperature contours during first 0.5 ms after opening of the valve at a speed of 20 m/s. (a) $t = 0.03$ ms, (b) $t = 0.04$ ms, (c) $t = 0.10$ ms, (d) $t = 0.15$ ms, (e) $t = 0.20$ ms, (f) $t = 0.30$ ms, and (g) $t = 0.50$ ms.

axis as it propagates into the driven section. Furthermore, the structure of the regular reflection waves can be seen between the central axis and the walls of the tube, propagating downstream of the FOV. It can be seen in the temperature contours that the contact surface is not planar, as it is under the influence of a vortex that mixes the driver and driven gases.

Fig. 15 shows the further evolution of the shock wave for the valve-opening speed of 10 m/s at 1.1 ms after the opening of the valve, when the shock wavefront is 1.4 m away from the FOV. The pressure contours show that the reflection waves become successively weaker as they propagate downstream of the FOV and the pressure distribution in the driven section becomes more homogeneous. The temperature contours show that the mixing effects around the contact surface are still present.

Fig. 16 shows a comparison of the pressure distributions along the cells near the wall of the shock tube at 3.5 ms after opening the valve at different speeds and the ideal 1-D theory. It is clear that the effects of the reflection waves, which result in the pressure peaks, are more prominent in the first meter downstream of the FOV. As can be seen from the position of the shock wavefront, the shock wave velocity increases with the opening speed of the valve, where the shock wave generated by the instantaneous opening of the valve exceeds the shock wave velocity predicted by the ideal 1-D theory.

In Fig. 17, the same comparison is made for the temperature distribution. It can be seen that the temperature in the high-temperature region is higher for higher opening speeds of the valve, whereas the temperature in the low-temperature region is similar for all the observed opening speeds. The transition between the cold and hot regions shows a similar behavior in all cases and the velocity of the contact surface is higher for higher opening speeds of the valve. If we compare the position of the contact surface for different cases with the position predicted by the ideal 1-D theory for that instant, we see that the velocity of the contact surface is, for opening speeds of the valve of 10 and 20 m/s, close to the velocity predicted by the ideal shock tube theory. On the other hand, the velocity of the contact surface for an opening speed of the valve of 5 m/s is lower and for the instantaneous opening of the valve it is higher than the velocity predicted by the ideal 1-D theory.

### *D. Shock Wave Velocity Along the Driven Section*

Fig. 18 shows that for all observed opening speeds of the valve, the shock wave velocity increases as the shock wave propagates away from the FOV. In the cases with finite opening speeds of the valve, the shock wave initially accelerates in proportion to the opening speed. The acceleration decreases shortly after 1-m downstream of the FOV. After this distance, the velocity of the shock wave continues to increase at an approximately constant rate for opening speeds of the valve of 5 and 10 m/s, although the rate of increase is smaller for an opening speed of 10 m/s. In contrast, for the shock wave generated at an opening speed of 20 m/s, the velocity is nearly constant between 1- and 2.3-m downstream of the FOV. After that, the velocity of the shock wave in this case decreases until two stronger pressure waves arrive, accelerating the shock front to a constant velocity. In the case of the instantaneous opening of the valve, the results show that the velocity of the shock wave reaches a constant value earlier than in the cases with finite opening speeds of the FOV. In this case, after

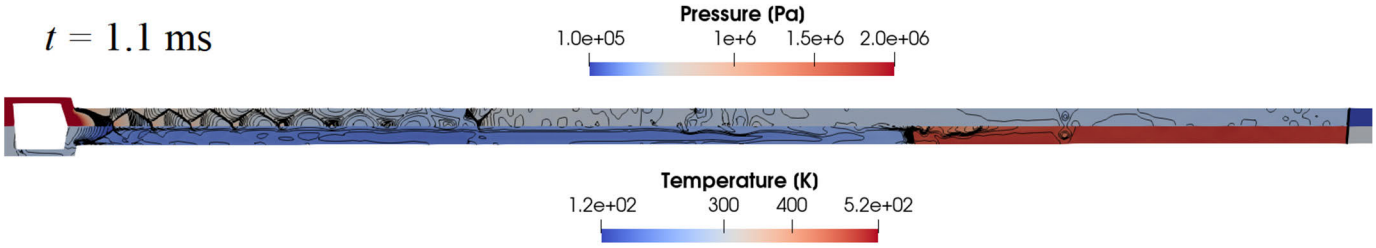


Fig. 15. Pressure and temperature contours at 1.1 ms after opening of the valve at a speed of 10 m/s.

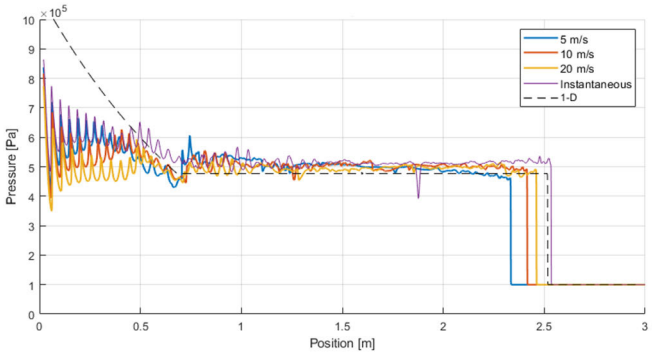


Fig. 16. Comparison of the pressure distribution along the driven section at 3.5 ms after opening the valve at different speeds and the ideal 1-D case.

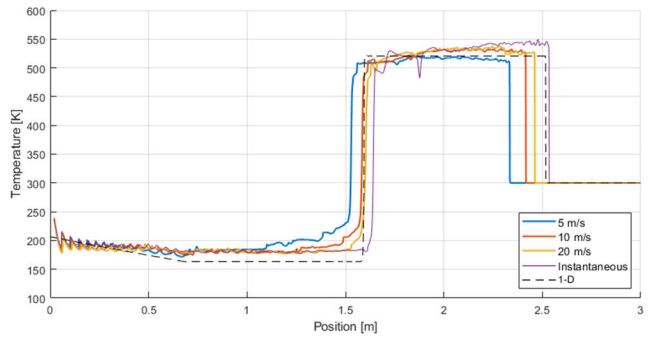


Fig. 17. Comparison of the temperature distribution along the driven section at 3.5 ms after opening the valve at different speeds and the ideal 1-D case.

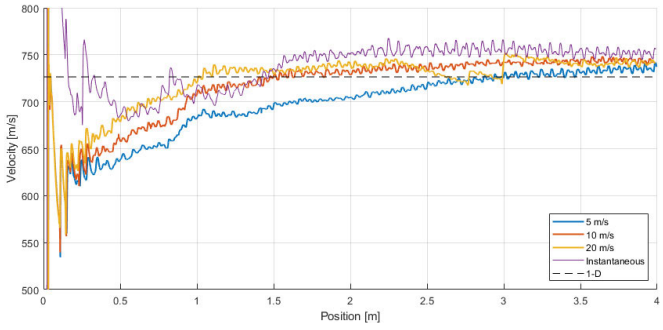


Fig. 18. Evolution of the shock wave velocity along the driven section.

2-m downstream of the FOV, the velocity of the shock wave stabilizes at a value that represents the limiting velocity of the shock wave for the cases with finite opening velocities of the valve. It is noticeable that after 3-m downstream of the FOV, the shock wave velocities for all the observed cases are higher

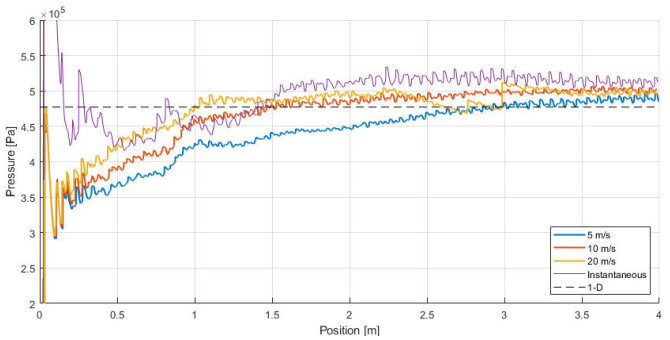


Fig. 19. Evolution of the pressure behind the shock wave along the driven section.

than those predicted by the ideal shock tube theory according to (15).

Fig. 19, which shows the pressure behind the shock wavefront during the formation distance, correlates well with Fig. 18, proving that the phenomenon of shock wave acceleration is indeed due to the increase in pressure behind the shock wavefront. The geometry of the FOV leads to a pressure amplification at the beginning of the driven section, where pressure waves of increasing strength are generated and propagate downstream at the speed of sound relative to the flow. Thus, these waves eventually coalesce into the leading shock and increase its velocity.

As shown in Figs. 18 and 19, the shock wave velocity and the pressure behind the shock wave show a similar oscillatory behavior for all the observed opening speeds. To investigate these oscillations, the pressure signals on the shock tube axis and at the wall 2.2-m downstream of the FOV for the case of the instantaneous opening of the valve were analyzed. As can be seen from Fig. 20, the passage of the shock wave causes an increase in the pressure, which is followed by pressure oscillations that are more prominent on the tube axis than at the wall due to the convergence of the radial pressure waves.

The frequencies of the oscillations in pressure shown in Fig. 21 were determined by applying a fast Fourier transform (FT) to 1 ms of the pressure signals after the pressure rise. The resulting amplitude spectra in Fig. 21 show the most distinctive peaks at about 23 kHz and their harmonics. The frequency of 23 kHz corresponds to the ratio of the acoustic speed of the pressure waves $u_2 + a_2$ (where $u_2$ and $a_2$ are the postshock flow velocity and the speed of sound, respectively) and the inner diameter of the shock tube. This frequency also corresponds to the lowest limiting frequency of the oscillations generated by the partially opened diaphragms in the diaphragm shock tubes [47].

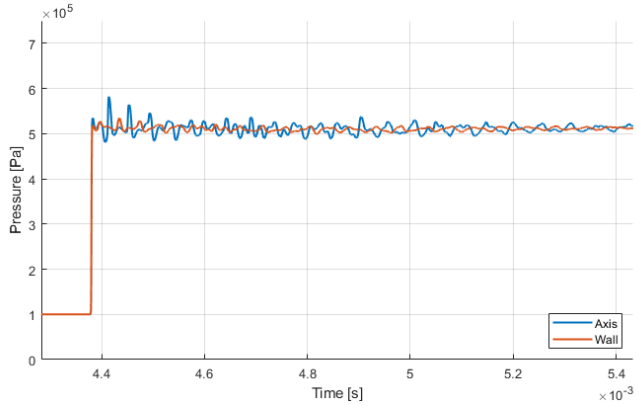


Fig. 20. Pressure signals on the axis and at the wall of the shock tube 2.2-m downstream of the FOV.

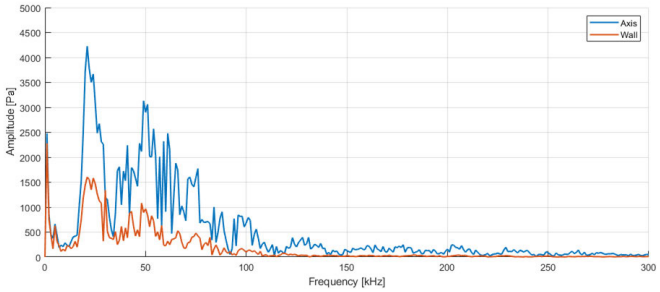


Fig. 21. Amplitude spectra of the pressure signals after the passage of the shock wave.

## V. Conclusion

This article presents a numerical study of the effects of the opening mechanism of the commercially available ISTA KB-40-100 FOV on the formation of a shock wave in the shock tube. Numerical simulations were performed in OpenFOAM for different opening speeds for the valve of 5, 10, and 20 m/s. These were compared with the instantaneous valve opening and the results predicted by the ideal shock tube theory.

The results show that the mass flow through the valve in general increases in proportion to the opening speed of the valve. When the mass flow reaches the steady maximum value, it remains constant until the expansion wave reflected from the end wall of the driver section reaches the valve. The results also show that the steady maximum mass flow through the valve increases with the opening speed of the valve.

The pressure and temperature contours along the driven section during the first moments of FOV opening show that due to the geometry of the FOV, a toroidal shock wave is generated that converges on the central axis of the shock tube. This results in an amplification of the shock wave upon its reflection from the axis, followed by successive reflections between the central axis and the walls of the shock tube. This creates a planar shock wavefront and a subsequent structure of reflection waves propagating into the driven section. The results for the shock wave velocity show that the shock wavefront accelerates more in the first meter downstream of the FOV with faster valve openings. After this distance, the shock wave velocities increase more slowly until they reach a limiting value determined by the instantaneous opening of the FOV. The effects of the reflection waves are present in all cases along the driven section and lead to an oscillating behavior of the shock wave velocity. To investigate these oscillations, two pressure signals were analyzed after the passage of the shock front. The analysis shows a dominance of the frequency of about 23 kHz, which corresponds to the lowest limiting frequency of the pressure oscillations generated by the partially opened diaphragms that has been determined in other studies. The oscillations of the shock wave velocity identified in this numerical study affect the accuracy of determining the shock wave velocity using a TOF method, which is required for determining the pressure step at the end wall of the driven section of the shock tube as the primary dynamic pressure calibration standard. In order to determine the distance from the FOV after which the boundary-layer effects begin to attenuate the shock wave velocity and its oscillations and thus the distance from the FOV after which the side-wall pressure sensors must be placed in order to determine the shock wave velocity with a lower uncertainty, the numerical model will be upgraded in the future by taking into account the thermal and viscous effects within the boundary layer.

## References

[1] J. D. Anderson Jr., *Fundamentals of Aerodynamics*, 6th ed. New York, NY, USA: McGraw-Hill, 2016.

[2] R. Camussi et al., "Wind tunnel measurements of the surface pressure fluctuations on the new VEGA-C space launcher," *Aerosp. Sci. Technol.*, vol. 99, Apr. 2020, Art. no. 105772.

[3] H. Qin and W. Wang, "Transient aerodynamic performances and pressure oscillations of a core engine combustor during start up," *Aerosp. Sci. Technol.*, vol. 115, Aug. 2021, Art. no. 106838.

[4] H.-L. Ding, S.-H. Yi, Y. Xu, and X.-H. Zhao, "Recent developments in the aero-optical effects of high-speed optical apertures: From transonic to high-supersonic flows," *Prog. Aerosp. Sci.*, vol. 127, Nov. 2021, Art. no. 100763.

[5] C. M. Grégoire et al., "Shock-tube spectroscopic CO and $H_2O$ measurements during 2-methyl-1-butene combustion and chemical kinetics modeling," *Combustion Flame*, vol. 238, Apr. 2022, Art. no. 111919.

[6] K. Takayama and T. Saito, "Shock wave/geophysical and medical applications," *Annu. Rev. Fluid Mech.*, vol. 36, pp. 347–379, Jan. 2004.

[7] K. Takayama and K. Ohtani, "Applications of shock wave research to medicine," *WIT Trans. Model. Simul.*, vol. 41, pp. 653–661, Jun. 2005.

[8] D. W. Holder and D. L. Schultz, *On the Flow in a Reflected-Shock Tunnel*. London, U.K.: Her Majesty's Stationery Office, 1962.

[9] A. Svete and J. Kutin, "Characterization of a newly developed diaphragmless shock tube for the primary dynamic calibration of pressure meters," *Metrologia*, vol. 57, no. 5, Sep. 2020, Art. no. 055009.

[10] Z. Yao, X. Liu, C. Wang, and W. Yang, "Improved traceable measurement of the reflected step pressure in shock tube with the compensation of shock wave attenuation," *Aerosp. Sci. Technol.*, vol. 107, Dec. 2020, Art. no. 106302.

[11] H. J. Pain and E. W. E. Rogers, "Shock waves in gases," *Rep. Prog. Phys.*, vol. 25, no. 1, pp. 287–336, Jan. 1962.

[12] V. E. Bean, "Dynamic pressure metrology," *Metrologia*, vol. 30, no. 6, pp. 737–741, Jan. 1994.

[13] J. Hjelmgren, "Dynamic measurement of pressure: A literature survey," SP Swedish Nat. Test. Res. Inst., Borås, Sweden, SP Rep. 2002:34, 2002.

[14] S. Downes, A. Knott, and I. Robinson, "Determination of pressure transducer sensitivity to high frequency vibration," in *Proc. IMEKO 22nd TC3, 12th TC5 3rd TC22 Int. Conf.*, Cape Town, South Africa, 2014, pp. 1–6.

[15] S. Downes, A. Knott, and I. Robinson, "Towards a shock tube method for the dynamic calibration of pressure sensors," *Phil. Trans. Roy. Soc. A, Math., Phys. Eng. Sci.*, vol. 372, no. 2023, Aug. 2014, Art. no. 20130299.

[16] S. Downes, A. Knott, and I. Robinson, "Uncertainty estimation of shock tube pressure steps," in *Proc. XXI IMEKO World Congr. Meas. Res. Ind.*, Prague, Czech Republic, 2015, pp. 1648–1651.

[17] F. R. F. Theodoro, M. L. C. D. C. Reis, C. D. Souto, and E. D. Barros, "Measurement uncertainty of a pressure sensor submitted to a step input," *Measurement*, vol. 88, pp. 238–247, Jun. 2016.
[18] C. Sarraf and J.-P. Damion, "Dynamic pressure sensitivity determination with Mach number method," *Meas. Sci. Technol.*, vol. 29, no. 5, Mar. 2018, Art. no. 054006.
[19] C. Sarraf, "A method for assessing the uncertainty of a secondary dynamic pressure standard using shock tube," *Meas. Sci. Technol.*, vol. 32, no. 1, Nov. 2020, Art. no. 015013.
[20] A. J. Knott and I. A. Robinson, "Dynamic characterisation of pressure transducers using shock tube methods," *J. Phys., Conf. Ser.*, vol. 1065, Aug. 2018, Art. no. 162002.
[21] J. N. D. S. Vianna, A. B. D. S. Oliveira, and J. P. Damion, "Influence of the diaphragm on the metrological characteristics of a shock tube," *Metrologia*, vol. 36, no. 6, pp. 599–603, Dec. 1999.
[22] E. Hanson, D. A. Olson, H. Liu, Z. Ahmed, and K. O. Douglass, "Towards traceable transient pressure metrology," *Metrologia*, vol. 55, no. 2, pp. 275–283, Mar. 2018.
[23] R. S. Hickman, L. C. Farrar, and J. B. Kyser, "Behavior of burst diaphragms in shock tubes," *Phys. Fluids*, vol. 18, no. 10, pp. 1249–1252, Oct. 1975.
[24] G. Persico, P. Gaetani, and A. Guardone, "Dynamic calibration of fast-response probes in low-pressure shock tubes," *Meas. Sci. Technol.*, vol. 16, no. 9, pp. 1751–1759, Jul. 2005.
[25] M. S. Hariharan, S. Janardhanraj, S. Saravanan, and G. Jagadeesh, "Diaphragmless shock wave generators for industrial applications of shock waves," *Shock Waves*, vol. 21, no. 3, pp. 301–306, Dec. 2010.
[26] A. M. Tulgestke, S. E. Johnson, D. F. Davidson, and R. K. Hanson, "High-speed imaging of inhomogeneous ignition in a shock tube," *Shock Waves*, vol. 28, no. 5, pp. 1089–1095, May 2018.
[27] E. Amer, M. Wozniak, G. Jönsson, and F. Arrhén, "Evaluation of shock tube retrofitted with fast-opening valve for dynamic pressure calibration," *Sensors*, vol. 21, no. 13, Jun. 2021, Art. no. 4470.
[28] S. Janardhanraj, S. K. Karthick, and A. Farooq, "A review of diaphragmless shock tubes for interdisciplinary applications," *Prog. Energy Combustion Sci.*, vol. 93, Nov. 2022, Art. no. 101042.
[29] S. Sembian and M. Liverts, "On using converging shock waves for pressure amplification in shock tubes," *Metrologia*, vol. 57, no. 3, Jun. 2020, Art. no. 035008.
[30] I. Hristov, A. Svete, and J. Kutin, "Vibrational effects on the dynamic pressure measurement standard based on a diaphragmless shock tube," *Meas., Sensors*, vol. 18, Dec. 2021, Art. no. 100116.
[31] A. Svete and J. Kutin, "Identifying the high-frequency response of a piezoelectric pressure measurement system using a shock tube primary method," *Mech. Syst. Signal Process.*, vol. 162, Jan. 2022, Art. no. 108014.
[32] A. Svete, F. J. H. Castro, and J. Kutin, "Effect of the dynamic response of a side-wall pressure measurement system on determining the pressure step signal in a shock tube using a time-of-flight method," *Sensors*, vol. 22, no. 6, p. 2103, Mar. 2022.
[33] E. Amer, G. Jönsson, and F. Arrhén, "Towards traceable dynamic pressure calibration using a shock tube with an optical probe for accurate phase determination," *Metrologia*, vol. 59, no. 3, Jun. 2022, Art. no. 035001.
[34] U. Planko, A. Svete, and J. Kutin, "Dynamic calibration of pressure sensors with the use of different gases in the shock tube," in *Proc. IMEKO 24th TC3, 14th TC5, 6th TC16 5th TC22 Int. Conf.*, Dubrovnik, Croatia, 2023, pp. 1–5.
[35] A. Svete, E. Amer, G. Jönsson, J. Kutin, and F. Arrhén, "A method for correcting the high-frequency mechanical vibration effects in the dynamic calibration of pressure measurement systems using a shock tube," *Mech. Syst. Signal Process.*, vol. 193, Jun. 2023, Art. no. 110246.
[36] J. Subburaj, T. A. Kashif, and A. Farooq, "Methane and n-hexane ignition in a newly developed diaphragmless shock tube," *Combustion Flame*, vol. 253, Jul. 2023, Art. no. 112818.
[37] J. H. Castro, A. Svete, and J. Kutin, "Numerical study of the effects of the separation-element configuration on the characteristics of a shock tube," *Meas., Sensors*, vol. 18, Dec. 2021, Art. no. 100101.
[38] E. W. Lemmon, I. H. Bell, M. L. Huber, and M. O. McLinden, "NIST standard reference database 23: Reference fluid thermodynamic and transport properties-REFPROP, version 10.0," Standard Reference Data Program, Nat. Inst. Standards Technol., Gaithersburg, MD, USA, 2018. [Online]. Available: https://www.nist.gov/srd/refprop, doi: 10.18434/T4/1502528.
[39] F. M. White, *Viscous Fluid Flow*, 3rd ed. New York, NY, USA: McGraw-Hill, 2006.
[40] B. E. Poling, J. M. Prausnitz, and J. P. O'Connell, *The Properties of Gases and Liquids*, 5th ed. New York, NY, USA: McGraw-Hill, 2001.
[41] S. Janardhanraj, K. Abhishek, and G. Jagadeesh, "Insights into the shockwave attenuation in miniature shock tubes," *J. Fluid Mech.*, vol. 910, Mar. 2021, Art. no. A3.
[42] R. Portaro, H. Nakayama, and H. D. Ng, "Analysis of a quick-acting diaphragmless shock tube driver," in *Proc. 29th Int. Symp. Shock Waves*, vol. 1, R. Bonazza and D. Ranjan, Eds. Cham, Switzerland: Springer, 2015, pp. 421–426.
[43] L. F. G. Marcantoni, J. P. Tamagno, and S. A. Elaskar, "High speed flow simulation using OpenFOAM," *Mecánica Comput.*, vol. 31, no. 16, pp. 2939–2959, Nov. 2012.
[44] G. D. van Albada, B. van Leer, and W. W. Roberts Jr., "A comparative study of computational methods in cosmic gas dynamics," *Astron. Astrophys.*, vol. 108, no. 1, pp. 76–84, Apr. 1982.
[45] J. D. Anderson, *Modern Compressible Flow: With Historical Perspective*, 3rd ed. New York, NY, USA: McGraw-Hill, 2003.
[46] E. M. Barkhudarov, M. O. Mdivnishvili, I. V. Sokolov, M. I. Taktakishvili, and V. E. Terekhin, "Mach reflection of a ring shock wave from the axis of symmetry," *J. Fluid Mech.*, vol. 226, pp. 497–509, May 1991.
[47] P. Gaetani, A. Guardone, and G. Persico, "Shock tube flows past partially opened diaphragms," *J. Fluid Mech.*, vol. 602, pp. 267–286, May 2008.

**Francisco Javier Hernández Castro** received the B.Sc. degree in aerospace engineering from Universidad Carlos III de Madrid, Madrid, Spain, in 2016, and the M.Sc. degree in aerospace science and technology from the Universitat Politècnica de Catalunya, Barcelona, Spain, in 2019. He is currently pursuing the Ph.D. degree with the Laboratory of Measurements in Process Engineering, Faculty of Mechanical Engineering, University of Ljubljana, Ljubljana, Slovenia.

He is a Researcher with the Laboratory of Measurements in Process Engineering. His research interests are concentrated on the development of a shock tube primary measurement standard for time-varying pressures, particularly on the effects related to shock wave velocity on the characteristics of such measurement standard.

**Jože Kutin** received the B.Sc. and Ph.D. degrees in mechanical engineering from the University of Ljubljana, Ljubljana, Slovenia, in 1996 and 2003, respectively.

He is an Associate Professor in metrology with the Faculty of Mechanical Engineering, University of Ljubljana, where he heads the Laboratory of Measurements in Process Engineering. His research interests include concentrated on the fluid flow metrology and the measurement dynamics of pressure and temperature sensors.

Dr. Kutin is an Associate Editor of *Flow Measurement and Instrumentation Journal*, in 2021.

**Andrej Svete** received the B.Sc. and Ph.D. degrees in mechanical engineering from the University of Ljubljana, Ljubljana, Slovenia, in 2007 and 2012, respectively.

He is an Assistant Professor in metrology and a Researcher with the Laboratory of Measurements in Process Engineering, Faculty of Mechanical Engineering, University of Ljubljana. His research interests are concentrated on the measurement dynamics of pressure sensors, the development of a primary standard for the dynamic calibration of pressure meters, and the dynamic signal processing.

Dr. Svete is a member of the Technical Committee on Pressure and Vacuum Measurement (TC16) of the International Measurement Confederation (IMEKO) in 2020.